01 Jan 2023

Compositional Modifications to Alter and Suppress Laves Phases in AlxCrMoTayTi Alloys

Austin E. Mann

Joseph William Newkirk
Missouri University of Science and Technology, jnewkirk@mst.edu

Recommended Citation

Compositional Modifications to Alter and Suppress Laves Phases in Al$_x$CrMoTa$_y$Ti Alloys

Austin E. Mann* and Joseph W. Newkirk

Herein, the development of refractory complex concentrated alloys in the Al–Cr–Mo–Ta–Ti alloy system is reported. Alloys with modified Al and Ta concentrations are designed using CALPHAD tools and produced via arc melting and characterized in both as-cast and annealed forms. Properties of the alloys, nature of the microstructures, and phase transformation behavior are described via X-ray diffraction, microstructural characterization, microhardness, and differential scanning calorimetry. Two alloys, namely, Al$_{0.25}$CrMoTa$_{0.8}$Ti and Al$_{0.75}$CrMoTa$_{0.8}$Ti, are represented by a body-centered-cubic matrix phase after annealing, along with a secondary Cr–Ta Laves phase of the C15 and C14 polytypes, respectively. In as-cast and annealed forms, the Al$_{0.75}$CrMoTa$_{0.45}$Ti alloy comprises a single-bcc phase. Microhardness of the Laves phase containing alloys demonstrates susceptibility to cracking, whereas the Al$_{0.75}$CrMoTa$_{0.45}$Ti alloy displays high specific hardness, signs of ductility as evidenced by slip traces near indentations, and minimal scatter of hardness values.

1. Introduction

The pursuit of high-speed flight presents critical challenges in the areas of thermal management, power generation, and vehicle performance and efficiency. Sophisticated concepts for airborne thermal management systems have been proposed[1] and are proposed for both airborne and terrestrial power generation systems.[2] Momentum in the development of novel technologies for high-speed flight is particularly demanding of current state-of-the-art materials, and, therefore, warrants significant effort in the maturation of novel alloying concepts for extreme environments. Survivability of materials subject to operation in these environments of course depends on their inherent transient strength and stability over the temperature range experienced, environmental resistance (considering oxidation and other possible environments such as supercritical CO_2), and

time-dependent properties (i.e., creep resistance) for long-term applications.

Complex concentrated alloys, and for that matter multiprincipal element alloys according to their broadest definition,[3] present a unique opportunity in the field of alloy development.[4–6] In particular, refractory complex concentrated alloys, or RCCAs, offer significant benefit to raise the temperature capability against traditional refractory alloying strategies, including lighter or more oxidation-resistant elements for the purpose of improving the overall performance of the alloy.

Environmental resistance of the base metal alloy is a key consideration for life of the component within an advanced thermal management system and as such was a driving factor in optimization of the alloy described herein. The AlCrMoTaTi system recently demonstrated a unique level of oxidation resistance up to 1100 °C, produced via sputter coating[7,8] and arc melting methods.[9]

Research in the field of aluminum-containing RCCAs is extensive, whereby the benefits of aluminum additions, including reduced alloy density, enhanced oxidation resistance, and improved ambient and elevated temperature strength, can be realized. Of course, aluminum can introduce challenges as well, preferentially forming intermediate phases, ordering of the matrix phase, reducing ductility, among others. Regardless, many researchers have still sought the inclusion of aluminum in RCCAs[10–12] and refractory superalloys.[13,14]

Yu et al. developed Al-containing refractory superalloys with dramatic elevated temperature strength improvements over MarM247,[14] and Stepanov et al.[11] and Senkov et al.[13] reported substantial specific strength improvements over a wide temperature range compared to many state-of-the-art precipitation hardened alloys, albeit with multiphase microstructures observed in some instances.

A single-phase structure was maintained in the Al$_{0.4}$Hf$_{0.6}$NbTaTiZr alloy[9] after solidification, annealing, and deformation. This was in partial agreement with thermodynamic predictions for that system, although some lower-temperature equilibrium phases that were predicted were in fact not observed.

Despite the exceptional oxidation resistance demonstrated by the Al–Cr–Mo–Ta–Ti alloy system, it is known to quite preferentially form a Cr–Ta Laves phase,[15] and recent substantial modifications to Al did not drastically alter the prevalence of the Laves phase,[16,17] while significant Ta modifications were necessary to rid the system of grain boundary Laves phase presence after

A. E. Mann
The Boeing Company
Boeing Research and Technology
St. Louis, MO 63134, USA
E-mail: austin.e.mann@boeing.com

A. E. Mann, J. W. Newkirk
Department of Materials Science and Engineering
Missouri University of Science and Technology
Rolla, MO 65409, USA

The ORCID identification number(s) for the author(s) of this article can be found under https://doi.org/10.1002/adem.202201614.

**ADVANCED
SCIENCE NEWS**

www.advancedsciencenews.com

**ADVANCED
ENGINEERING
MATERIALS**

www.aem-journal.com

homogenization and cooling.[18] However, reasonable correlation was found between thermodynamic predictions and observed phase transformations,[16] leading to confidence in further potential optimization of the system. Tuning Al and Cr ratios in the AlCrMoTaTi system was demonstrated, whereby sophisticated ordered structures could be directed, although these modifications did not demonstrate a disordered solid solution.[19] In relatable work on the AlCrMoNbTi alloy system, lattice distortion effects on numerous high entropy alloys (HEAs) were validated, including also the AlCrMoTi system which appeared as single-phase body-centered cubic (bcc) disordered structure in initial studies.[20] Disordered structures were later confirmed only in low-aluminum concentrations ($\leq$5 at%) in the AlCrMoTi quaternary system, with ordering well correlated by thermodynamic calculations.[21]

Interestingly in other complex alloy systems, aluminum additions have managed to stabilize the bcc structure.[22] Related work has also sought to identify correlations for room-temperature ductility of RCCAs,[23] which for refractory alloys is a common crux due to ductile-to-brittle transition temperatures near room temperature and up to several 1000 °C, hindering low-temperature processing and performance of these alloys.

In the present work, further modifications based on thermodynamic calculations of the AlCrMoTaTi system resulted in the $Al_{0.25}CrMoTa_{0.8}Ti$, $Al_{0.75}CrMoTa_{0.8}Ti$, and $Al_{0.75}CrMoTa_{0.45}Ti$ alloys.[24] In prior work, we studied the effect of minor alterations of Al and Ta, at first to examine the effect on possibly intermetallic phase formation, which eventually led to presumptions of other outcomes, including stability of the bcc phase, alteration of oxidation resistance, and reduced alloy cost. Previous modifications to the AlCrMoTaTi alloy system revealed that less than 15 at% Al reduces the potency of $CrTaO_4$ formation during oxidation at 1200 °C, whereby rapid oxidation of Al at or near the surface allows for easier diffusion of Cr and formation of Cr_2O_3 and critical $CrTaO_4$ layers.[17] In addition, Ta modifications demonstrated that <10 at% is also critical to oxidation at 1200 °C, in which MoO_3 evaporation can accelerate and deficiencies of Ta do not support sustained growth of the $CrTaO_4$ intermediate layer, which itself slows diffusion and additional ingress of oxygen into the AlCrMoTaTi metal substrate.[18]

Thus, this research reports on the optimization of modified compositions in the AlCrMoTaTi alloy system. Outcomes of this work led to a better understanding of requirements to optimize the structural potential of this alloy system and also create the opportunity to study effects on oxidation behavior of the alloys in future work.

2. Theory and Calculation

Initial thermodynamic calculations in this system focus on refined approaches based on CALPHAD results from prior work,[16] as well as other work that specifically evaluated the dependencies of Al, Cr, and Ta.[17–19] In this research, a critical driver for the success of the alloy includes long-term environmental and microstructural stability at 1000 °C.[2] As such, particular emphasis was placed on the equilibrium behavior of the alloy at this temperature as well as in the annealing regime (1300 °C). The dependency of equilibrium phases on Al and

Ta concentrations at the two temperatures of interest in the Al–Cr–Mo–Ta–Ti system, in which Al and Ta concentration variations correlate to equally balanced amounts of remaining alloying elements in the system, has been previously explained.[16] Although prior work thermodynamically favored the sigma phase as the second-most prevalent high-temperature phase in this alloy system, it has not been observed experimentally, and, therefore, was practically excluded from calculations to hopefully improve predictability of the behavior of Laves phases. At 1300 °C, the Laves phase exhibits a strong dependence on Al, suggesting that the Laves phase might dissolve at higher aluminum concentrations. However, this was not found to be the case in prior experimental results.[16,19] In contrast, adjustments to the Ta concentration have very little effect on maintaining a possibly ordered bcc structure at this high annealing temperature. Equilibrium calculations at 1000 °C reveal similar tendencies for Al dependence on cubic forms of the Laves phase, including precipitation of a mu phase at lower concentrations, which is yet to be substantiated with experimental evidence. Calculations of Ta dependence at 1000 °C suggest that reducing the Ta concentration should decrease the volume fraction of Laves phases, which generally agrees with prior experimental findings and considerations of the composition of the Laves phase itself in this system.

Given the aforementioned capacity of Al and Ta on phase equilibrium in this quaternary system, it was necessary to the authors to examine combinatorial effects on the total system. Therefore, three described alloys were conceived for this work: $Al_{0.25}CrMoTa_{0.8}Ti$, $Al_{0.75}CrMoTa_{0.8}Ti$, and $Al_{0.75}CrMoTa_{0.45}Ti$. In combination, these alloys drastically altered the Al concentration in an attempt to increase the probability of a disordered matrix, while significantly modifying Ta concentrations to reduce the likelihood of Laves-phase precipitation. The precise amounts of Al and Ta in each of the three alloys were determined based on approximate Laves-free corridors and local maxima for the bcc matrix phase.

One-axis equilibrium calculations over the broad temperature range of 600–2000 °C are given for each of the three alloys, as shown in **Figure 1**. The $Al_{0.25}CrMoTa_{0.8}Ti$ alloy still maintains a fair amount of the C15 Laves phase up to just below 1400 °C. The $Al_{0.75}CrMoTa_{0.8}Ti$ alloy calculations predict a slightly better outcome, resulting in a single-phase bcc matrix in the annealing range and yet still nearly 80% bcc at 1000 °C. Predominant secondary phases are either the C14 (hexagonal) or C15 (cubic) Laves phases, which seem to trade off from one another at lower temperatures. Finally, the $Al_{0.75}CrMoTa_{0.45}Ti$ alloy remains a single-phase bcc alloy down to almost 1100 °C, and also at 1000 °C is still nearly 85% bcc, which is the most promising calculation of this family of modified alloys. The main secondary phase is the C14 Laves phase, which has a calculated dissolution temperature in this alloy just above 1000 °C.

3. Results and Discussion

3.1. Microstructure and Hardness

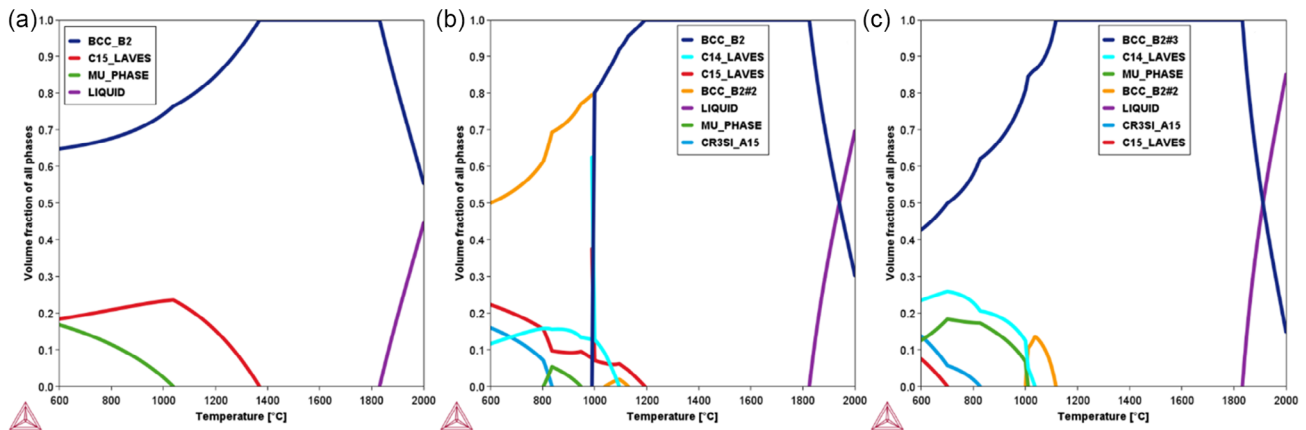Chemistries of the thrice-melted products were analyzed by ICP–OES, and results are shown in **Table 1**. Measured

ADVANCED
SCIENCE NEWS

www.advancedsciencenews.com

ADVANCED
ENGINEERING
MATERIALS

www.aem-journal.com

Figure 1. One-axis equilibrium calculation of each alloy as a function of temperature: a) $Al_{0.25}CrMoTa_{0.8}Ti$, b) $Al_{0.75}CrMoTa_{0.8}Ti$, and c) $Al_{0.75}CrMoTa_{0.45}Ti$. Each alloy exhibited widely varying Laves phase dissolution temperatures, although similar solidus temperatures are noted across all alloys. The $Al_{0.75}CrMoTa_{0.45}Ti$ alloy displays a wide range of bcc phase stability above 1000 C, and a fairly low C14 Laves phase dissolution temperature compared to the other alloys.

Table 1. Measured chemical composition via ICP–OES (in at%) of the as-cast alloys.

Alloy	Al	Cr	Mo	Ta	Ti
$Al_{0.25}CrMOTa_{0.8}Ti$	6.0	26.0	24.8	15.6	27.6
$Al_{0.75}CrMOTa_{0.8}Ti$	15.4	24.3	21.6	13.8	24.9
$Al_{0.75}CrMOTa_{0.45}Ti$	15.1	26.4	23.6	8.1	26.8

chemistries of the alloys are in appropriate agreement with the intended compositions, deviating by less than 2 at% for each element in all alloys, except for Ta content in the $Al_{0.75}CrMoTa_{0.8}Ti$, which was 2.2 at% less than the intended composition. Estimated densities of the alloys were calculated by the Equation

$$\rho_{estimated} = \frac{\sum c_i A_i}{\sum \frac{c_i A_i}{\rho_i}} \quad (1)$$

where c_i is the atomic percentage of an element, A_i is the atomic weight of an element, and ρ_i is the density of the pure element. Estimated densities are 8.46 g cc^{-1} for the $Al_{0.25}CrMoTa_{0.8}Ti$ alloy, 7.80 g cc^{-1} for the $Al_{0.75}CrMoTa_{0.8}Ti$ alloy, and 7.20 g cc^{-1} for the

$Al_{0.75}CrMoTa_{0.45}Ti$ alloy. It should be noted that one-axis equilibrium calculations presented in the previous section were based on the measured chemical compositions presented; however, the nominal compositions were retained in the alloy's nomenclature for ease of maintaining specimen traceability and such.

Microstructures of the arc-melted alloys are shown in **Figure 2**. In the as-melted condition, the alloys exhibit highly dendritic structures. Dark features are noted in each microstructure, which in some instances appear to be remnant microporosity from the arc melting process, as well as Ti-rich features that were determined by energy dispersive spectroscopy (EDS) to also be rich in nitrogen (not shown). As discussed in previous work,[16] it was determined that the presence of the TiN did not have a substantial impact on thermodynamic behavior of the alloys and the availability of Ti to contribute to the equilibrium behavior of the system, due to low volume fraction of TiN and the amount of Ti it would ultimately segregate from the system to precipitate the nitride.

Backscatter electron images and associated EDS maps of the subject alloys in annealed condition are shown in **Figure 3–5**. The annealed microstructure of the $Al_{0.25}CrMoTa_{0.8}Ti$ alloy (Figure 3) consists of many finely dispersed needle-like features, inhabiting intragranular regions in the microstructure. These are
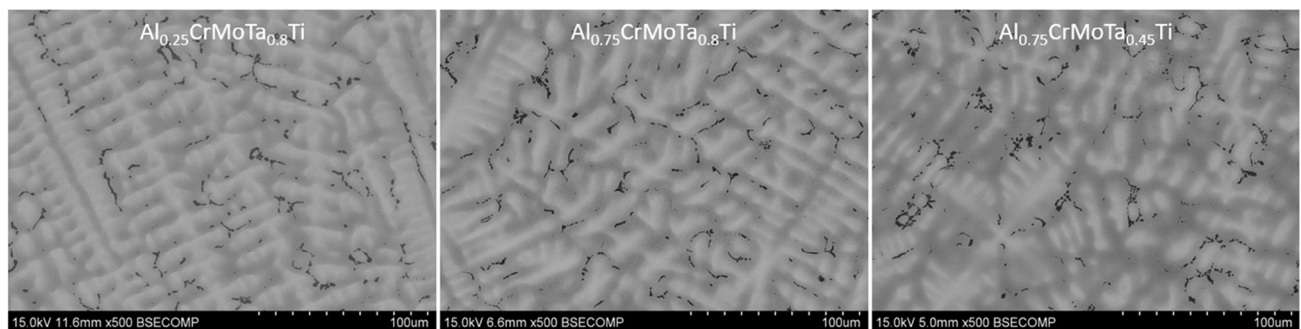

Figure 2. Microstructures of the as-cast alloys. No significant differences in the as-cast state are noted between the three alloys. Black features are in some instances microporosity, but mostly TiN inclusions.
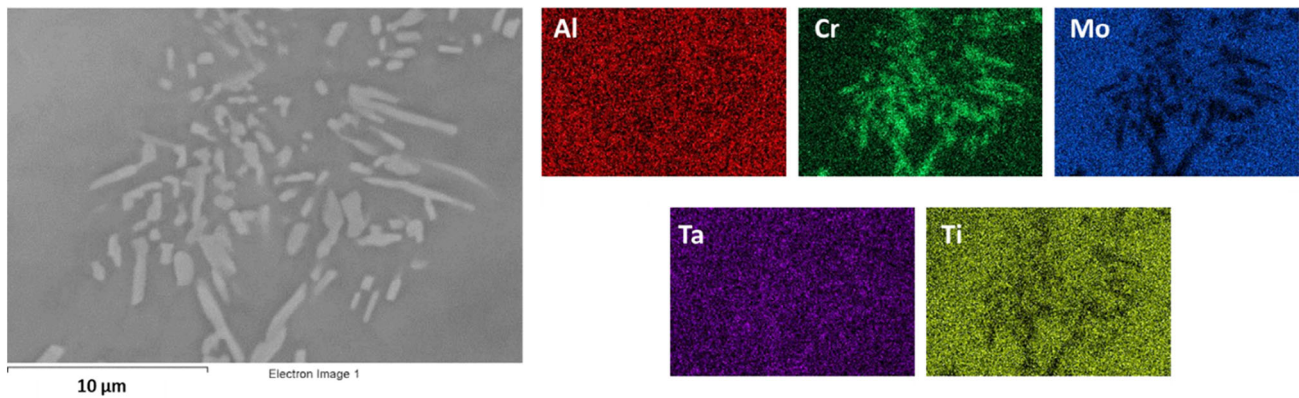
**ADVANCED
SCIENCE NEWS**

www.advancedsciencenews.com

**ADVANCED
ENGINEERING
MATERIALS**

www.aem-journal.com

Figure 3. BSE image and associated EDS maps of the annealed $Al_{0.25}CrMoTa_{0.8}Ti$ alloy. Intragranular Cr– and Ta–rich features are the Laves phase, and the surrounding matrix has a fairly homogeneous distribution of remaining elements.
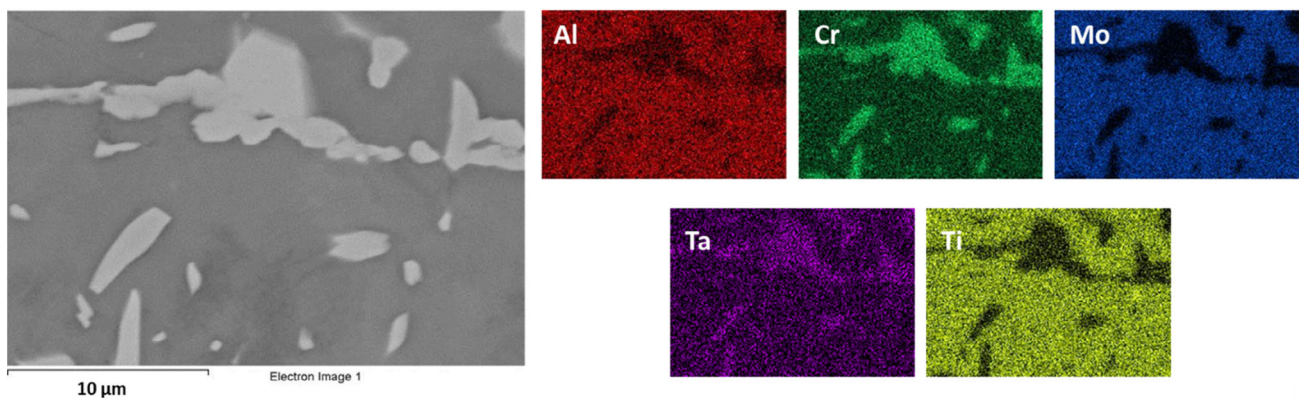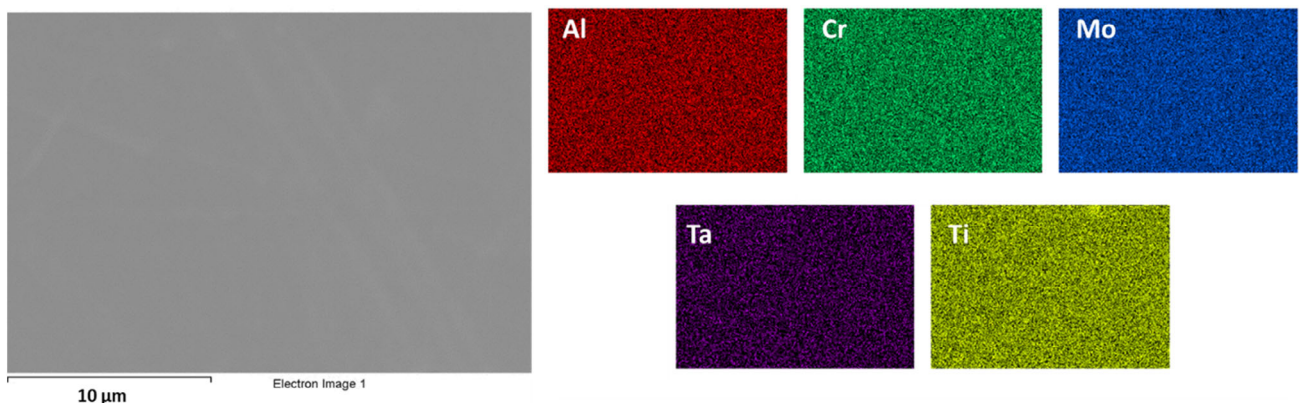

Figure 4. BSE image and associated EDS maps of the annealed $Al_{0.75}CrMoTa_{0.8}Ti$ alloy. Similarly, intragranular Cr- and Ta-rich features are the Laves phase, and the surrounding matrix has a fairly homogeneous distribution of remaining elements.

Figure 5. BSE image and associated EDS maps of the annealed $Al_{0.75}CrMoTa_{0.45}Ti$ alloy. No Laves features were observed, and the singular matrix phase has a homogeneous distribution of the principal alloying elements.

of course Cr and Ta rich as evidenced by the EDS maps shown, presumably a Laves phase. Microstructure of the annealed $Al_{0.75}CrMoTa_{0.8}Ti$ alloy is shown in Figure 4, and consists of coarse and block intragranular features, as well as several micrometer-thick intergranular necklace features. EDS maps also reveal these to be significantly enriched in Cr and Ta, again presumably Laves phase. Finally, the annealed $Al_{0.75}CrMoTa_{0.45}Ti$ microstructure (Figure 5) is devoid of any secondary phases and is a uniform matrix with homogeneous distribution of elements.
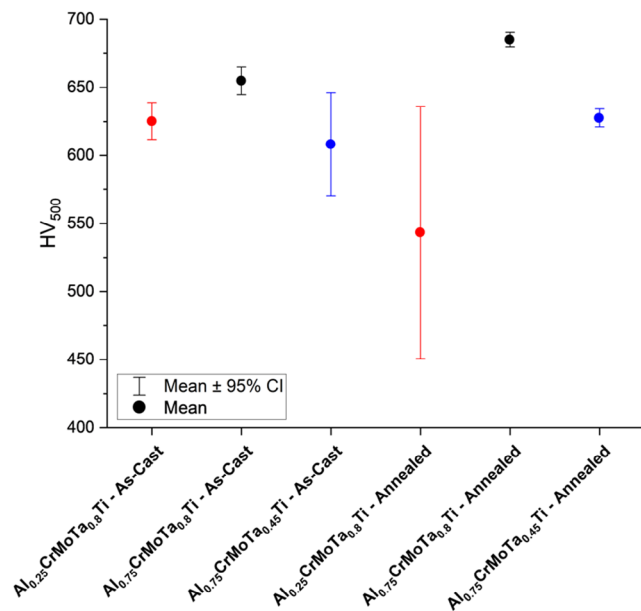
Figure 6. Microhardness results of the as-cast and annealed alloys. Note the reduction in scatter for annealed alloys, except for the wide scatter in the $Al_{0.25}CrMoTa_{0.8}Ti$ alloy due to significant cracking of indentations. Specific hardness of the annealed $Al_{0.75}CrMoTa_{0.8}Ti$ and $Al_{0.75}CrMoTa_{0.45}Ti$ alloys is quite high (≈ 87 HV cm^{-3} g^{-1}).

Microhardness results from the as-cast and annealed alloys are shown in **Figure 6**. The results comprise a distribution of 6–10 indentations in each specimen. Hardness values for the as-cast $Al_{0.25}CrMoTa_{0.8}Ti$ alloy were distributed fairly tightly (average ≈ 625 HV), while in the annealed condition, the hardness was much more widely distributed (average ≈ 543 HV), particularly due to cracking during indentation and high volume fraction of the brittle Laves phase. Average hardness values for the as-cast (≈ 655 HV) and annealed states (≈ 685 HV) of the $Al_{0.75}CrMoTa_{0.8}Ti$ alloy were much more similar, with the annealed alloy exhibiting slightly higher average hardness by about 30 HV, but much less cracking susceptibility compared to the $Al_{0.25}CrMoTa_{0.8}Ti$ alloy. The $Al_{0.75}CrMoTa_{0.45}Ti$ alloy also exhibited fairly high average hardness values in the as-cast (≈ 608 HV) and annealed conditions (≈ 627 HV). The lower

hardness in the as-cast condition for the latter two alloys is likely due to the dendritic microstructure and remnant chemical heterogeneity. In the annealed state, each alloy generally exhibits a more chemically homogeneous matrix, albeit with secondary phases detrimental to mechanical behavior. Mean specific hardness (HV/ρ) of the annealed $Al_{0.75}CrMoTa_{0.8}Ti$ and $Al_{0.75}CrMoTa_{0.45}Ti$ alloys was ≈ 87.8 and 87.2 HV cm^3 g^{-1}, respectively. Images of select representative microhardness indentations are shown in **Figure 7** for each annealed alloy. Severe cracking is noted in the annealed $Al_{0.25}CrMoTa_{0.8}Ti$ alloy (Figure 7a), possibly along a Laves phase-rich boundary. Significant cracking is also noted in the example $Al_{0.75}CrMoTa_{0.8}Ti$ annealed alloy indentation (Figure 7b), however with some minor slip traces observed in the matrix phase. Indentations in the single-phase-annealed $Al_{0.75}CrMoTa_{0.45}Ti$ alloy are rather clean (Figure 7c), despite the noted TiN inclusions. Slip traces are evident in several directions through the microstructure, suggesting that this alloy in the present condition may exhibit some room-temperature ductility, which could be confirmed by future compression or tensile testing. Ultra-high specific hardness of these alloys is promising for their potential specific strength.

XRD patterns of the as-cast alloys are shown in **Figure 8**, and each diffraction pattern for the as-cast alloys is indicative of a single bcc phase. It is again worth noting for this work that the thermodynamic calculations presented beforehand did not predict a disordered bcc phase, but rather the B2 phase and further ordered subvariants denoted B2#2 or B2#3. In similar Al–Cr–Mo–Ti alloys, it was clearly demonstrated that XRD may not be able to fully resolve the possibility of very weak superlattice site occupation[21] and, therefore, ordering of the bcc matrix. For these alloys, we must consider this to also be possible and, therefore, plan for future transmission electron microscopy (TEM) studies to confirm this behavior. The diffraction patterns of the as-cast alloys as shown are indeed indicative of a single bcc phase in their present condition, however with some peak broadening and even signs of overlapping peaks at the higher diffraction angles in the $Al_{0.25}CrMoTa_{0.8}Ti$ (Figure 8—red curve) and $Al_{0.75}CrMoTa_{0.8}Ti$ (Figure 8—black curve) alloys. At higher diffraction angles, these overlapping peaks could coincide with B2-ordered reflections (especially near 73° and 87°), indicating that weak ordering might be present upon solidification. The possible presence of ordered bcc constituents is apparently dealt
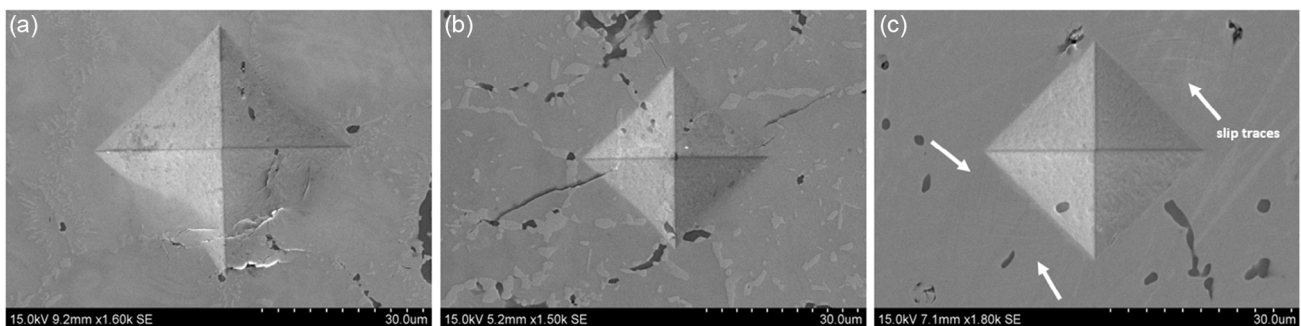

Figure 7. Select microhardness indent images from annealed alloys, a) $Al_{0.25}CrMoTa_{0.8}Ti$, b) $Al_{0.75}CrMoTa_{0.8}Ti$, and c) $Al_{0.75}CrMoTa_{0.45}Ti$. Note the cracking at corners and edges of indentations in (a,b). In (c), the $Al_{0.75}CrMoTa_{0.45}Ti$ alloy exhibits slip traces outward from indentations indicating some ductility.
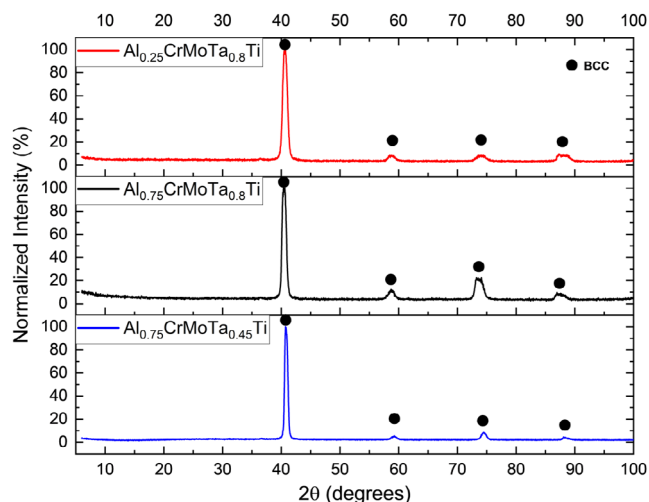
Figure 8. XRD patterns of the as-cast alloys. Peaks for all alloys were consistent with a single bcc phase.

away with by long-term annealing, as shown by sharpened peaks in **Figure 9**.

XRD patterns of the annealed alloys are shown in Figure 9. For the identified bcc phase in the annealed alloys, calculated lattice parameters are 3.169 Å ($Al_{0.25}CrMoTa_{0.8}Ti$), 3.146 Å ($Al_{0.75}CrMoTa_{0.8}Ti$), and 3.146 Å ($Al_{0.75}CrMoTa_{0.45}Ti$). Two distinct Laves phase polytypes are identified in the $Al_{0.25}CrMoTa_{0.8}Ti$ (C15—cubic) and $Al_{0.75}CrMoTa_{0.8}Ti$ (C14—hexagonal) alloys. Initial scans of the annealed $Al_{0.75}CrMoTa_{0.8}Ti$ alloy did not clearly indicate which form of the Laves phase was present; however, an additional scan at increased count time (10 s) per step over the range of 35°–75° (see inset in **Figure 10**) resulted in better resolution of minor peaks, which confirmed the presence of the C14 Laves phase. Interestingly, the $Al_{0.75}CrMoTa_{0.45}Ti$ alloy diffraction pattern is

indicative of a single-phase bcc alloy after annealing. This combined reduction of Al and Ta to produce a single bcc phase is so far consistent with previous hypotheses, in that substantial reductions of Ta are necessary to avoid Cr–Ta-based Laves phases in this system, and minor reductions of Al may also contribute to this behavior, while also possibly preventing ordering of the bcc phase. As discussed, XRD is not indicating occupation of superlattice sites, but future TEM could confirm or deny this finding. For now, this is assumed this to be a single-disordered bcc phase.

The resulting microstructures and confirmed identity of secondary phases in these annealed alloys are worth comparing to thermodynamic predictions. Equilibrium calculations for the $Al_{0.25}CrMoTa_{0.8}Ti$ alloy in fact correctly predict the C15 polytype to be the prominent secondary phase at 1300 °C. Predicted volume fraction of the C15 phase at that temperature is about 8%, which seems to be an underprediction upon examination of the microstructure. Calculations of the $Al_{0.75}CrMoTa_{0.8}Ti$ alloy predict both the C14 and C15 at higher temperatures, although 100% bcc phase is calculated above 1200 °C, which is obviously not the case. Of course, the $Al_{0.75}CrMoTa_{0.45}Ti$ alloy represents the most favorable thermodynamic prediction, with 100% bcc phase predicted just above 1100 °C. In this alloy, the dominant secondary phase at temperatures below this is the C14 Laves phase, precipitation of which to this point has been avoided. Obviously, precise agreement between thermodynamic calculations and resultant microstructures is not demonstrated for this alloy system, but one could argue that general trends related to the identity and presence of secondary phases and regions of single-phase stability are fairly agreeable.

3.2. Differential Scanning Calorimetry

Thermograms of the on-heating behavior of the as-cast and annealed alloys are shown in Figure 10. The significant difference in magnitude of heat flow between the as-cast and annealed alloys can be attributed to microsegregation of alloying elements
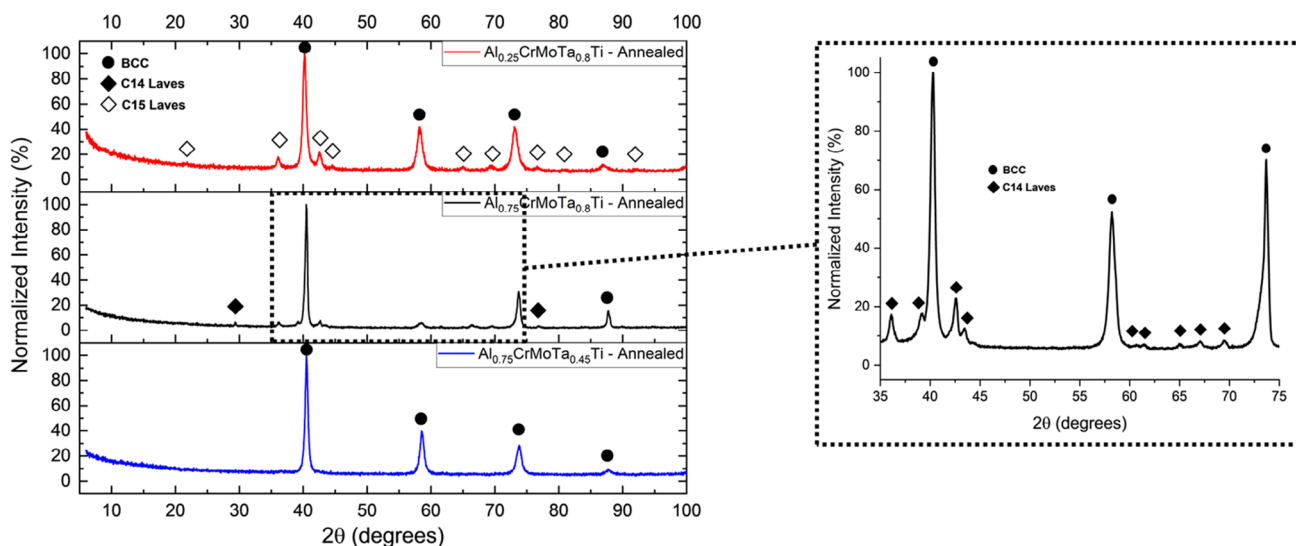

Figure 9. XRD patterns of the annealed alloys. Peaks in the $Al_{0.25}CrMoTa_{0.8}Ti$ and $Al_{0.75}CrMoTa_{0.8}Ti$ were consistent with a bcc matrix phase and the C15 and C14 Laves phase, respectively. Only bcc phase peaks are noted in the $Al_{0.75}CrMoTa_{0.45}Ti$ alloy.
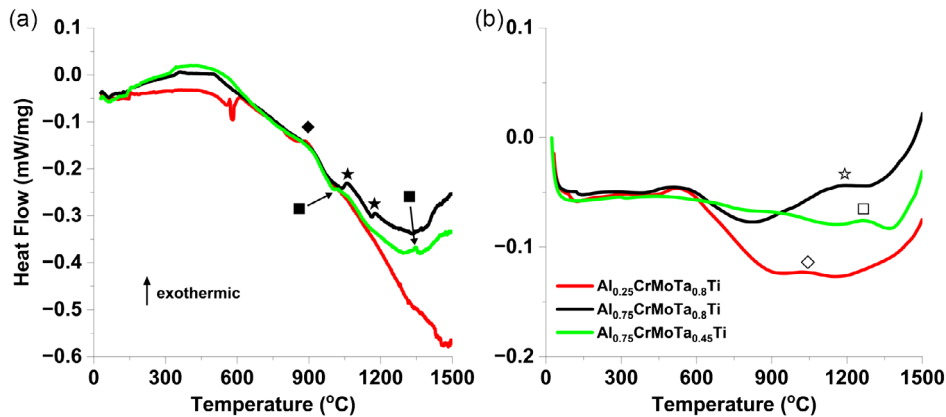
Figure 10. DSC results from heating of the a) as-cast and b) annealed alloys. Heating rate for all tests was 10 °C min^{-1}. Behavior of the as-cast alloys supported annealing at 1300 °C, and resulting exothermic peaks of the annealed alloys were compared to the ordering transition temperatures and Laves phase dissolution temperatures from thermodynamic calculations.

in the as-cast condition and necessary energy required to enable diffusion and subsequent transformations in those microstructures. Of course, in the annealed condition, thermograms exhibit much less variability in heat flow over the temperature range. Exothermic behavior consistent with melting onset above 1400 °C in the as-cast material is possibly due to lower solidus temperatures, again due to microsegregation effects prior to high-temperature annealing treatments. Thermograms of the as-cast alloys rationalized an annealing temperature of 1300 °C, such that minimal thermal events occurred in this temperature range, and thermodynamic tools calculated this to be a single-phase bcc region.

The $Al_{0.25}CrMoTa_{0.8}Ti$ alloy exhibits a single exothermic peak at 880 °C (aside from the anomaly noted at 560 °C which could not be correlated to ordering or phase transformations) in the as-cast condition (see the black diamond marker in Figure 10a), while the annealed form of the alloy exhibits a single peak at 1050 °C (white diamond marker in Figure 10b). The as-cast $Al_{0.75}CrMoTa_{0.8}Ti$ alloy exhibits two peaks at 1060 and 1170 °C (black star markers in Figure 10a), and the annealed condition exhibits a rather broad peak with an apparent local maximum around 1177 °C (white star marker in Figure 10b). Finally, the $Al_{0.75}CrMoTa_{0.45}Ti$ alloy possesses two peaks in the as-cast condition at 1020 and 1350 °C (black square markers in Figure 10a), and similarly a broad high-temperature peak with a local maximum around 1275 °C (white square marker in Figure 10b). Peaks, as shown in Figure 10a, at 880 °C for the $Al_{0.25}CrMoTa_{0.8}Ti$ alloy, 1060 °C for the $Al_{0.75}CrMoTa_{0.8}Ti$ alloy, and 1020 °C for the $Al_{0.75}CrMoTa_{0.45}Ti$ alloy each appear lambda shaped, indicative of discontinuous ordering transformations. The highest temperature peaks, as shown in Figure 10a, for each alloy are slightly more symmetrical, as are the peaks of the annealed alloys, as shown in Figure 10b, indicative of continuous transformations and in the case of this system very likely the Laves phase precipitation temperatures.

Correlation between the thermodynamic predictions, as shown in Figure 2 and thermograms of the assumed equilibrium annealed state of these three alloys, is sporadic at best. A C15 Laves phase precipitation temperature is predicted in the $Al_{0.25}CrMoTa_{0.8}Ti$ alloy at nearly 1400 °C, which does not

correspond well to the lone local exothermic event described near 1050 °C. The exothermic peak of the $Al_{0.75}CrMoTa_{0.8}Ti$ alloy at 1177 °C is much more agreeable with predicted C14 and C15 Laves phase precipitation temperatures between 1100 and 1200 °C. Based on XRD results, this is believed to be the C14 Laves phase precipitation point. A very weak local exothermic peak in the thermogram of the annealed $Al_{0.75}CrMoTa_{0.45}Ti$ alloy about 1275 °C does not correlate properly with predictions of a C14 Laves precipitation at about 1025 °C. Thermodynamic calculations also estimate an ordering transformation just above 1100 °C in this alloy. It is interesting to observe the single-phase bcc behavior especially for the $Al_{0.75}CrMoTa_{0.45}Ti$ alloy, particularly if the local exothermic event at 1275 °C (just below the applied annealing temperature of 1300 °C) is related to a secondary Laves phase. Given that the other alloys studied also resulted in precipitation of a Laves phase while exhibiting quite similar Laves phase precipitation points says something about the sensitivity of Laves phase precipitation in this composition to temperature and possibly cooling rate. The results also lend themselves to questions surrounding the nature of these thermal events and if they are indeed related to ordering transformations as thermodynamic prediction tools suggest. Such behavior has been observed in similar complex alloys, although higher-fidelity microscopy is needed to confirm these hypotheses.

4. Conclusion

Development of a series of alloys with modified Al and Ta concentrations in the Al–Cr–Mo–Ta–Ti was presented, and the following conclusions are drawn: 1) A single-phase alloy was achieved through substantial Ta reduction and minor Al modification in the $Al_{0.75}CrMoTa_{0.45}Ti$ alloy, confirmed by XRD and microstructural characterization; 2) Multiple polytypes of the Cr–Ta Laves phase were present after annealing in the $Al_{0.25}CrMoTa_{0.8}Ti$ and $Al_{0.75}CrMoTa_{0.8}Ti$ alloys, also confirmed by XRD and microstructural analysis; 3) Differential scanning calorimetry (DSC) results of the developed alloys loosely agreed with trends in thermodynamic calculations for key phase transformations, giving a passable level of confidence in the use of

thermodynamic modeling platforms for alloy design in this system; and 4) The ability to achieve a single phase in this alloy system with promising hardness values and preliminary signs of room-temperature ductility provide momentum for future study of this alloy system and characterization of additional properties and performance metrics.

5. Experimental Section

Thermodynamic-phase equilibrium calculations were performed in Thermo Calc 2022 using the TCHEA5 thermodynamic database. All alloys were produced via arc melting from high-purity elemental powder feedstocks. Arc-melted ingots ≈50 g each were produced for each alloy. The purity and particle size of the feedstock powders were as follows: Al (>99%), Cr (99.99%, −60 mesh), Mo (99.9%, <150 μm), Ta (99.98%, −100 mesh), and Ti (99.4%, −100 mesh). Powders were mixed and cold compacted into briquette preforms for melting. Alloys were vacuum arc melted in an inert atmosphere on a water-cooled copper hearth and titanium chips were melted in the final atmosphere prior to melting to ensure minimal oxygen content in the melting environment. The alloys were flipped and remelted three times to ensure homogeneity, and melting resulted in ingots measuring ≈50 mm long × 12 mm wide × 3 mm tall. Alloy chemistry was determined by inductively coupled plasma–optical emission spectroscopy (ICP-OES). Heat treatment was performed in a Centorr Vacuum Industries Workhorse II Series 3530 vacuum heat treat furnace at 1300 °C for 24 h at 0.9×10^{-6} Torr and subsequently cooled to room temperature at 30 °C min^{-1}. Calorimetric data were acquired in yttria-coated alumina crucibles on a Netzsch DSC 404C Pegasus at a heating rate of 10 °C min^{-1} to 1500 °C in flowing argon. X-ray diffraction (XRD) patterns of bulk specimens were collected on a PANalytical X'Pert Pro multipurpose diffractometer instrument using Cu Kα radiation and a 2θ scattering angle from 6° to 100°, a step size of 0.03° per step, and 2 s per step. Secondary-electron and backscattered electron images were acquired on an FEI Quanta 400. Energy-dispersive X-ray elemental distribution maps were collected on a Hitachi S-3700 N. Microhardness was performed on a LECO LM248AT using a Vickers diamond indenter with a 500 g load.

Conflict of Interest

The authors declare no conflict of interest.

Data Availability Statement

Research data are not shared.

[1] M. F. Stoia, G. W. Ek, K. G. Bowcutt, J. T. Needels, in *AIAA Propulsion and Energy Forum*, American Institute of Aeronautics and Astronautics, Inc., August **2021**, https://doi.org/10.2514/6.2021-3531.

[2] A. Yousefiani, in *2022 ARPA-E HITEMMP Annual Review Meeting*, March **2022**, https://arpa-e.energy.gov/2022-hitemmp-annual-review-meeting.

[3] N. Birbilis, S. Choudhary, J. R. Scully, M. L. Taheri, *npj Mater. Degrad.* **2021**, *5*, 14.

[4] D. B. Miracle, O. N. Senkov, *Acta Mater.* **2017**, *122*, 448.

[5] O. N. Senkov, D. B. Miracle, K. J. Chaput, J.-P. Couzinie, *J. Mater. Res.* **2018**, *33*, 3092.

[6] N. R. Philips, M. Carl, N. J. Cunningham, *Metall. Mater. Trans. A* **2020**, *51A*, 3299.

[7] D.-C. Tsai, Z.-C. Chang, B.-H. Kuo, M.-H. Shiao, S.-Y. Chang, F.-S. Shieu, *Appl. Surf. Sci.* **2013**, *282*, 789.

[8] D.-C. Tsai, M.-J. Deng, Z.-C. Chang, B.-H. Kuo, E.-C. Chen, S.-Y. Chang, F.-S. Shieu, *J. Alloys Compd.* **2015**, *647*, 179.

[9] B. Gorr, F. Müller, M. Azim, H.-J. Christ, T. Müller, H. Chen, A. Kauffmann, M. Heilmaier, *Oxid. Met.* **2017**, *88*, 339.

[10] O. N. Senkov, S. V. Senkova, C. Woodward, *Acta Mater.* **2014**, *68*, 214.

[11] N. D. Stepanov, N. Yu Yurchenko, V. S. Sokolovsky, M. A. Tikhonovsky, G. A. Salishchev, *Mater. Lett.* **2015**, *161*, 136.

[12] O. N. Senkov, S. Gorsse, D. B. Miracle, *Acta Mater.* **2019**, *175*, 394.

[13] O. N. Senkov, D. Isheim, D. N. Seidman, A. L. Pilchak, *Entropy* **2016**, *18*, 102.

[14] X. H. Yu, Y. Yamabe-Mitarai, Y. Ro, H. Harada, *Metall. Mater. Trans. A* **2000**, *31A*, 173.

[15] F. Müller, B. Gorr, H.-J. Christ, H. Chen, A. Kauffmann, S. Laube, M. Heilmaier, *J. Alloys Compd.* **2020**, *842*, 155726.

[16] A. E. Mann, J. W. Newkirk, *Adv. Eng. Mater.* **2023**, 2201449, https://doi.org/10.1002/adem.202201449.

[17] S. Schellert, B. Gorr, H.-J. Christ, C. Pritzel, S. Laube, A. Kauffmann, M. Heilmaier, *Oxid. Met.* **2021**, *96*, 333.

[18] S. Schellert, B. Gorr, S. Laube, A. Kauffmann, M. Heilmaier, H.-J. Christ, *Corros. Sci.* **2021**, *192*, 109861.

[19] S. Laube, S. Schellert, A. S. Tirunilai, D. Schliephake, B. Gorr, H.-J. Christ, A. Kauffmann, M. Heilmaier, *Acta Mater.* **2021**, *218*, 117217.

[20] H. Chen, A. Kauffmann, S. Laube, I.-C. Choi, R. Schwaiger, Y. Huang, K. Lichtenberg, F. Müller, B. Gorr, H.-J. Christ, M. Heilmaier, *Metall. Mater. Trans. A* **2018**, *49A*, 772.

[21] S. Laube, H. Chen, A. Kauffmann, S. Schellert, F. Müller, B. Gorr, J. Müller, B. Butz, H.-J. Christ, M. Heilmaier, *J. Alloys Compd.* **2020**, *823*, 153805.

[22] J. Y. He, W. H. Liu, H. Wang, Y. Wu, X. J. Liu, T. G. Nieh, Z. P. Lu, *Acta Mater.* **2014**, *62*, 105.

[23] O. N. Senkov, D. B. Miracle, S. I. Rao, *Mater. Sci. Eng., A* **2021**, *820*, 141512.

[24] A. E. Mann, A. Yousefiani, J. W. Newkirk, United States Patent and Trademark Office Filing No. 17/808,629. Patent Pending.